processes

MDPI

Article

A Possible Explicit Equation Fitting Method for the Gaseous Heat Capacity Near the Critical Point Based on Density and Temperature

Mukun Li [1,*], Gang Wang [1], Lulu Sun [1], Xiaoqiang Cao [1] and Hongjian Ni [2]

[1] College of Safety and Environmental Engineering, Shandong University of Science and Technology, Qingdao 266590, China
[2] School of Petroleum Engineering, China University of Petroleum (East China), Qingdao 266580, China
* Correspondence: limukun@sdust.edu.cn

Abstract: CO_2 is a potential fluid for absorbing and accumulating thermal energy; an accurate and fast calculation method for the heat capacity is essential for the study of the flow state near the critical point. However, the calculation of the heat capacity near the critical point by the equations suggested by NIST can easily be divergent, such as for CO_2, nitrogen, methane, etc. Therefore, an explicit fitting equation was studied. The fitting equation, which used density and temperature as variables and contained three constants, was derived from the nature of heat capacity change (molecular kinetic energy and potential energy). Based on the heat capacity data of the NIST WebBook, the heat capacity of CO_2 is taken as the example for the equation deduction and parameter fitting. The three constants were defined in order by Origin fitting software. By this new approach, it is found that the heat capacity at the critical point is below 1% deviant from that of the NIST WebBook. Moreover, the heat capacities that are difficult to be calculated in the NIST WebBook are well calculated. The study shows that the fitting equation is efficient for the prediction of heat capacity of gases near the critical point.

Keywords: heat capacity; molecular kinetic energy; molecular potential energy; fitting; explicit equation

Citation: Li, M.; Wang, G.; Sun, L.; Cao, X.; Ni, H. A Possible Explicit Equation Fitting Method for the Gaseous Heat Capacity Near the Critical Point Based on Density and Temperature. *Processes* **2023**, *11*, 1605. https://doi.org/10.3390/pr11061605

Academic Editor: Federica Raganati

Received: 13 April 2023
Revised: 16 May 2023
Accepted: 22 May 2023
Published: 25 May 2023

1. Introduction

Supercritical carbon dioxide (SC-CO_2 for short) can produce large temperature differences with pressure changes near the critical point. Therefore, it has become an effective medium for jet rock breaking, fracturing, thermal cycling, and other deep earth resource exploitation technologies. SC-CO_2, as a jet medium, can improve the mechanical penetration rate, increase oil and gas production, save water resources and energy, and reduce emissions, and it has become an anhydrous drilling fluid and fracturing fluid with great application potential [1–3]. The threshold pressure of the SC-CO_2 jet for breaking granite and shale is two-thirds and one-half that of a water jet, respectively [4]. SC-CO_2 coiled-tubing slim-hole jet-assisted rock breaking drilling can greatly reduce the drilling cost due to the low threshold pressure of jet rock breaking, low circulating pressure loss, the improved service life of drilling tools, and accessible underbalanced drilling conditions [4,5]. Compared with water jet fracturing, the initiation pressure of SC-CO_2 jet fracturing is less than half of that of water jet fracturing [6]. With SC-CO_2 as the fracturing fluid, clay hydration and expansion as well as water shortage can be solved. Moreover, shale has stronger adsorption of CO_2, which can replace methane and realize CO_2 geological storage [7–10]. The common basic problem in SC-CO_2 jet drilling and SC-CO_2 jet fracturing is the mechanism of the SC-CO_2 jet rock breaking. At present, a lot of experiments on SC-CO_2 jet rock breaking have been conducted, proving that SC-CO_2 jets have greater advantages than water jets in rock breaking [4,5,11–16]. What is interesting about the mechanism is that a large temperature gradient and high-temperature stress can be generated under a SC-CO_2 jet, and the higher

temperature stress is the main reason why the SC-CO_2 jet is superior to the water jet in rock breaking [17–20]. Nevertheless, there are few studies on the SC-CO_2 jet flow field and stress field near the critical point due to the drastic changes in density, heat capacity, etc.

Geothermal and solar electricity generation is a renewable generating technology that can enable significant reduction in fossil fuel consumption. In environmental, cost, and safety terms, CO_2 is regarded as an ideal natural heat transfer medium [21–28]. The SC-CO_2-based Brayton cycle has been seen as a good alternative to conventional power cycles because of high cycle efficiency, compact turbo machinery, and compact heat exchangers [29–33]. The big change in SC-CO_2 heat capacity near the critical point makes it efficient to store and release energy. If we control the CO_2 phase of flow under the supercritical state, there will be no phase change such as water gasification and the cost of the equipment controlling phase change can be saved [29]. Moreover, the heat transfer rate is high near the critical point [34–36]. Based on the theory above, Ni et al. have successfully applied invention patents using SC-CO_2 near critical point as a transmission media to more efficiently generate electricity [37] and make use of geothermal resources to supply heating and exploit oil [38]. As the patents described, the cycle efficiency of SC-CO_2 near the critical point is more than two times that of water in the conditions where the energy of water vaporization can be transferred to electricity 100%. The main problem is how to predict and control the flow state near the critical point. Simulation is a good method for flow prediction and design of the experimental setup.

Recently, drug processing using SCFs has been proposed as a sufficient alternative for conventional techniques. SC-CO_2 is non-toxic, low-cost, non-flammable, and easyily accessible with moderate critical pressure and near ambient critical temperature. Amongst SCFs, SC-CO_2 and the mixtures containing high amounts of SC-CO_2 are the most used SCFs. Modeling is an efficient method for the study of drug solubilities and drug particle formation and delivery [39,40]. To predict the temperature, pressure, density, and velocity of fluids in the wide range of operating conditions, equations of density and heat capacity have an important effect on the accurate correlative capability [41].

In a word, the application of SC-CO_2 in the above technical fields is closely related to the fluid properties and flow field of carbon dioxide. Mature commercial software such as FLUENT and CFX are efficient and economical methods to study the flow field, and the heat capacity is an essential input parameter. For the accurate calculation of the heat capacity of carbon dioxide and its mixture, NIST real gas equations, such as the Span–Wagner (S-W) equation of state [42] and GERG-2008 wide-range equation [43], can satisfy both the calculation accuracy and application range in engineering. In addition, NIST has provided an effective software named REFPROP for the fluid properties calculation of density, heat capacity, and so on. However, although the FLUENT and NIST WebBook [44] used the same real gas equations for the calculation of isobaric heat capacity (C_p for short), such as those for carbon dioxide, methane, nitrogen, and water, the heat capacity near the critical point can easily diverge in the fluent simulation and NIST WebBook calculation (as shown in Table 1). By exploring the deep reason, one possible reason is that because the heat capacity calculation equation is implicit and involves multiple intermediate coefficients, if the significant digit of the parameter is reduced for the sake of fast calculation, numerical truncation and cumulative error will be generated, resulting in the situation that the heat capacity cannot be calculated.

Table 1. Points where critical heat capacities diverge easily in the NIST WebBook [44].

Fluid	Temperature (K)	Pressure (MPa)	ρ (kg/m^3)	*C*p (J/g·K)	Phase
CO_2	303.7	7.3725	608.81298	undefined	liquid
CO_2	304.2	7.3675	362.24288	undefined	vapor
CO_2	304.5	7.3835	342.33699	undefined	supercritical
CH_4	190.1	4.5955	214.82531	undefined	liquid
CH_4	190.6	4.5960	131.59005	undefined	vapor
CH_4	190.8	4.6035	122.47476	undefined	supercritical

Table 1. *Cont.*

Fluid	Temperature (K)	Pressure (MPa)	ρ (kg/m^3)	*C*p (J/g·K)	Phase
N_2	125.7	3.396	428.58276	undefined	liquid
N_2	126.2	3.392	255.06112	undefined	vapor
N_2	126.4	3.4	230.87678	undefined	supercritical
H_2O	646.6	22.064	423.77596	undefined	liquid
H_2O	647.2	22.06	250.46303	undefined	vapor
H_2O	647.5	22.066	230.395	undefined	supercritical

In terms of the gas heat capacity calculation, researchers have conducted a lot of valuable research. For example, C N Yang and C P Yang studied the critical point in the liquid–gas transition effect on the heat capacity of oxygen and noble gases [45]. W Botch and M Fixman founded a theory for dynamic heat capacity associated with long-wavelength density fluctuations in the critical region [46]. G Orkoulas et al. established that the divergence is shared almost equally between the second temperature derivatives of the pressure and the chemical potential [47]. Previous studies have shown that the heat capacity increases substantially near the critical point and density fluctuation and temperature-related parameters are the key factors affecting the heat capacity of gases. Therefore, this study derives the fitting equation method to directly solve the isobaric heat capacity calculation equation by density and temperature based on the authentic NIST WebBook data [44] and the nature of the heat capacity change (molecular kinetic energy and potential energy). The heat capacity of CO_2 is taken as the example for the equation deduction and parameter fitting. Compared with the existing implicit function equation for solving the heat capacity, this new explicit method is simpler and faster because the intermediate coefficients calculation is omitted and lots of iterative calculations are avoided. The heat capacity near the critical point is hard to diverge because of the smaller truncated cumulative error. Additionally, it gives a simple method for deducing the critical heat capacity by fitting the experimental data near the critical region. In particular, the current equations of states, namely the Peng–Robinson (PR), Soave–Redlich–Kwong (SRK), etc., can calculate the density, temperature, and pressure of gases, but there are no effective corresponding heat capacity equations. Therefore, the heat capacity calculation method established in this paper can also be an important supplement to the above gases' equations of state.

2. Identification of the Heat Capacity Fitting Equation

The internal energy of gas molecules can be divided into two parts, molecular kinetic energy and molecular potential energy, among which molecular kinetic energy is mainly related to the temperature. The isobaric heat capacity of fluids with constant density can be calculated according to Equation (1):

$$C_p = \frac{\Delta E_p + \Delta E_k}{\Delta T} \tag{1}$$

where C_p is the isobaric heat capacity, E_p is the molecular potential energy, E_k is the molecular kinetic energy, and T is the temperature.

The identification of the potential energy function is the key to determine the fitting of Equation (1), and the potential energy function can be divided into the model fluid potential energy function, the semi-empirical potential energy function, and the ab initio potential energy function [48]. In these three types of functions, the semi-empirical potential energy function is more welcome and popular due to its good calculation precision and simple form. The commonly used empirical potential energy model can be further divided into the two-center Lennard-Jones plus quadrupole model (2CLJQ) [49–52] and the three-center Lennard-Jones plus quadrupole model (3CLJQ) [53]. Among these two models, 2CLJQ was introduced for accurate simulation and calculation of the properties of supercritical carbon dioxide [54]. In addition, Meng Long et al. proposed a 2CLJDQP model considering the

long-range electrostatic and induction effects [55], and Wang Sheng et al. improved the 2CLJDQP model by introducing potential energy parameters related to temperature [56].

Molecular potential energy can be mainly divided into intermolecular potential energy and intramolecular potential energy. It is found that intermolecular attraction plays a more important role when the pressure is low, and then the fluid density fluctuates obviously, whereas the intermolecular repulsive force leads to weak density fluctuation when the pressure is high [57]. As the heat capacity is mainly influenced by density, intramolecular potential energy is not considered in this study, which can also simplify the fitting process. Although the later developed models such as 2CLJDQP have higher accuracy, they will make the fitted equations and processes more complicated. The intermolecular potential energy of 2CLJQ can be expressed by Equation (2) [58,59]; it has been proved to be useful for the isobaric heat capacity of working fluid in a supercritical CO_2 Brayton cycle. Since it is a function of density and temperature, the molecular potential energy is exclusively related to the temperature when the density is constant. The main purpose of considering potential energy is to obtain a semi-empirical formula based on the principles of a simple form and few parameters for fitting; the relationship of the energy and size terms of the 2CLJQ model to critical points [60] is also ignored.

$$E_{p(r,T)} = \frac{\varepsilon^{(eff)}}{n-6}\left\{6\left[\frac{{r_m}^{(eff)}}{r}\right]^n - n\left[\frac{{r_m}^{(eff)}}{r}\right]^6\right\} \tag{2}$$

where $\varepsilon^{(eff)}$ is the potential well depth determined by the temperature, ${r_m}^{(eff)}$ is the molecular equilibrium spacing determined by the temperature, r is the intermolecular spacing, and n is a constant.

$\varepsilon^{(eff)}$ and ${r_m}^{(eff)}$ can be approximately expressed as Equations (3) and (4).

$$\varepsilon^{(eff)} = \varepsilon\left(\frac{r_m}{{r_m}^{(eff)}}\right)^6 \tag{3}$$

$${r_m}^{(eff)} = r_m + dT \tag{4}$$

where ε and r_m are the potential well depth and the molecular equilibrium spacing, respectively, whereas d is a constant.

If we substitute Equations (3) and (4) into Equation (2), we can obtain Equation (5), which expresses the relationship between molecular potential energy and temperature. When the intermolecular distance is constant, Equation (5) is derivative, which can bring us Equations (6) and (7) that describe the variation in molecular potential energy and density potential energy with temperature, respectively.

$$E_{p(r,T)} = \frac{\varepsilon {r_m}^6}{n-6}\left(6\frac{(r_m+dT)^{n-6}}{r^n} - \frac{n}{r^6}\right) \tag{5}$$

$$\frac{\Delta E_{p(r,T)}}{\Delta T} = \frac{\partial E_{p(r,T)}}{\partial T} = \frac{6\varepsilon {r_m}^6 d^{n-6}(r_m/d+T)^{n-7}}{r^n} \tag{6}$$

$$\frac{\Delta E_{p(\rho,T)}}{\Delta T} = \frac{6\varepsilon\rho^{n/3}N^{n/3-2}d^{n-6}\left[(M/\rho_m)^{1/3}/d+T\right]^{n-7}}{{\rho_m}^2 M^n} \tag{7}$$

In Equation (7), ρ is the fluid density, N is the molar constant, M is the molecular weight, and ρ_m is the fluid density when molecules are in the ground state.

When the density is constant, all the parameters except the temperature in Equation (7) are constant. Therefore, Equation (7) can be simplified as a relationship involving three constants, a, T_0, and c, as shown in Equation (8).

$$\frac{\Delta E_{p(\rho,T)}}{\Delta T} = \frac{a}{(T - T_0)^c} \tag{8}$$

$$a = \frac{6\varepsilon\rho^{n/3}N^{n/3-2}d^{n-6}}{\rho_m{}^2 M^n} \tag{9}$$

$$T_0 = -(M/\rho_m)^{1/3}/d \tag{10}$$

$$c = 7 - n \tag{11}$$

The influence of the molecular kinetic energy on heat capacity can be neglected at the critical point because heat capacity significantly varies there and molecular potential energy dominants. In order to verify the correctness of Equation (8), the heat capacities of methane, water, nitrogen, and carbon dioxide under the critical density are fitted (corresponding to Figures 1–4, respectively). Table 2 displays the fitting values, determination coefficients (*R-square*), and mean absolute relative error (*MARE*) of the parameters in Equation (8). It is found that though the molecular kinetic energy is not considered, Equation (8) well applies the heat capacity near the critical temperature, demonstrating the effectiveness of the fitting near the critical point. However, as the temperature rises, the fitting error becomes bigger, finally resulting in a big absolute relative error.

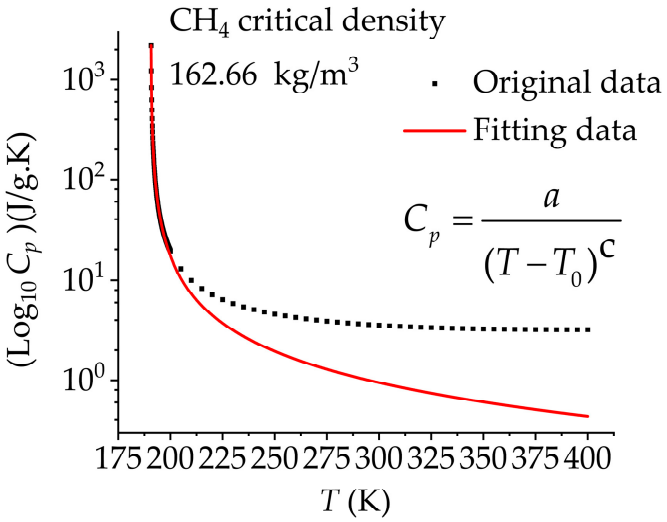

Figure 1. Original CH_4 heat capacity and fitting curve with the critical density of 162.66 kg/m^3 (without consideration of the molecular kinetic energy).

The molecular kinetic energy cannot be neglected anymore when the temperature is away from the critical point, as it contributes more to the heat capacity when the effect of the molecular potential energy decreases. Figures 5 and 6 show the fitting results of the CO_2 heat capacity with densities of 10 kg/m^3 and 50 kg/m^3, from which we can further find that Equation (8) is not applicable for the fitting far away from the fluid critical point.

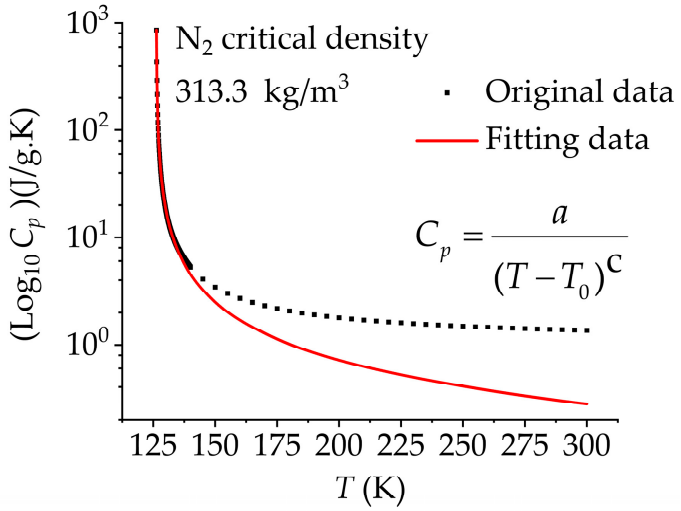

Figure 2. Original N_2 heat capacity and fitting curve with the critical density of 313.3 kg/m^3 (without consideration of the molecular kinetic energy).

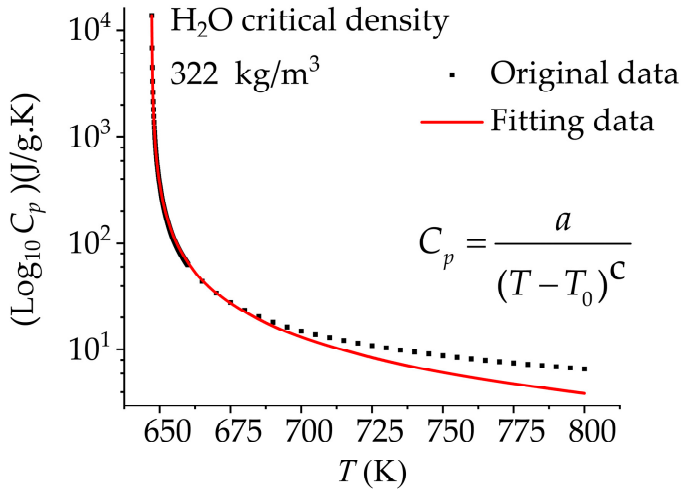

Figure 3. Original H_2O heat capacity and fitting curve with the critical density of 322 kg/m^3 (without consideration of the molecular kinetic energy).

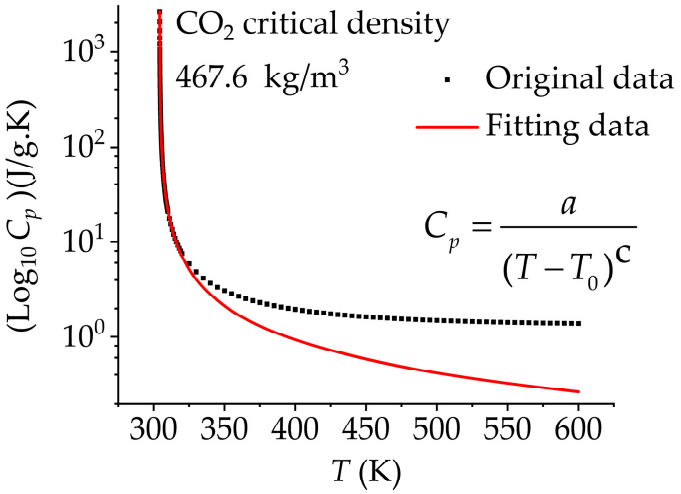

Figure 4. Original CO_2 heat capacity and fitting curve with the critical density of 467.6 kg/m^3 (without consideration of the molecular kinetic energy).

Table 2. Fitting results of critical heat capacity with different fluids.

Fluid	Critical Density kg/m^3	*a*	*c*	T_0	*R-Square*	*MARE* (%)
CH_4	162.66	247.6514	1.18539	190.5413	0.99993	90.2242
N_2	313.3	81.74206	1.10026	126.1819	0.99993	41.4713
H_2O	322	1228.679	1.14402	647.0782	0.99995	27.5464
CO_2	467.6	156.7309	304.1184	1.12325	0.99997	65.2738

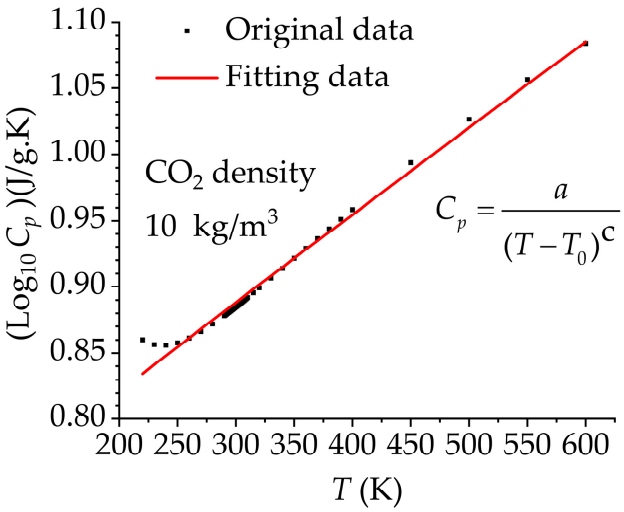

Figure 5. Original CO_2 heat capacity and fitting curve with the density of 10 kg/m^3 (without consideration of the molecular kinetic energy).

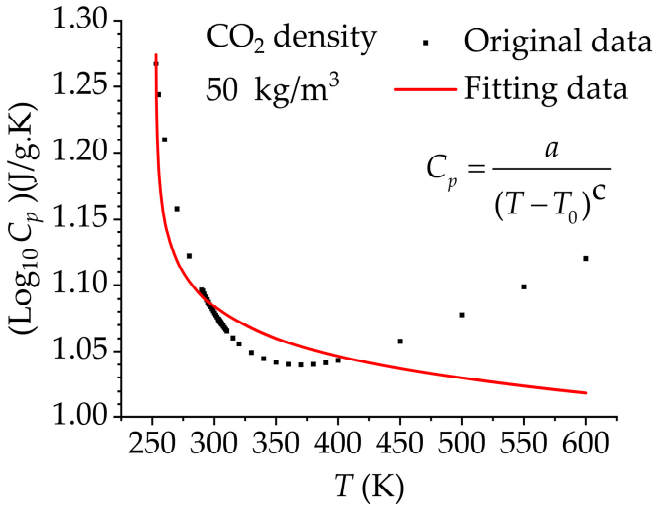

Figure 6. Original CO_2 heat capacity and fitting curve with the density of 50 kg/m^3 (without consideration of the molecular kinetic energy).

It has been demonstrated that the molecular kinetic energy can be approximately calculated by the regression of a one-variable polynomial equation [61,62]. By the law that explains the variation in the molecular potential energy with the distance to the molecules [63], we can know that the molecular potential energy rarely varies with the temperature when the intermolecular distance is very large; therefore, the variation in heat capacity can be regarded as the variation in molecular kinetic energy with temperature.

We use the CO_2 heat capacity corresponding to density of 0.0001 kg/m^3 to approximate the change in CO_2 kinetic energy per unit mass. Then, based on the calculation data of the NIST WebBook [44], we employed OriginPro to fit the relationship between CO_2 kinetic

energy and temperature (as shown in Equation (12)) with a determination coefficient of 0.99999. Next, we substitute Equations (12) and (8) into Equation (1) and can obtain the CO_2 heat capacity fitting Equation (13).

$$\frac{\Delta E_k}{\Delta T} = Cp_{\rho\,=\,0.0001} = 0.58496 - \frac{2.10229T}{10^4} + \frac{8.49535T^2}{10^6} - \frac{2.36752T^3}{10^8} + \frac{2.84159T^4}{10^{11}} - \frac{1.29972T^5}{10^{14}} \quad (12)$$

$$Cp_{CO_2} = \frac{a}{(T - T_0)^c} + 0.58496 - \frac{2.10229T}{10^4} + \frac{8.49535T^2}{10^6} - \frac{2.36752T^3}{10^8} + \frac{2.84159T^4}{10^{11}} - \frac{1.29972T^5}{10^{14}} \quad (13)$$

Equation (13) is then used to again test the CO_2 heat capacity fitting effect. Figures 7 and 8 are the CO_2 heat capacity fitting curves considering molecular kinetic energy with respective densities of 10 kg/m^3 and 50 kg/m^3. It is obvious that Equation (13), which considers molecular kinetic energy, can well fit the CO_2 heat capacity with low density.

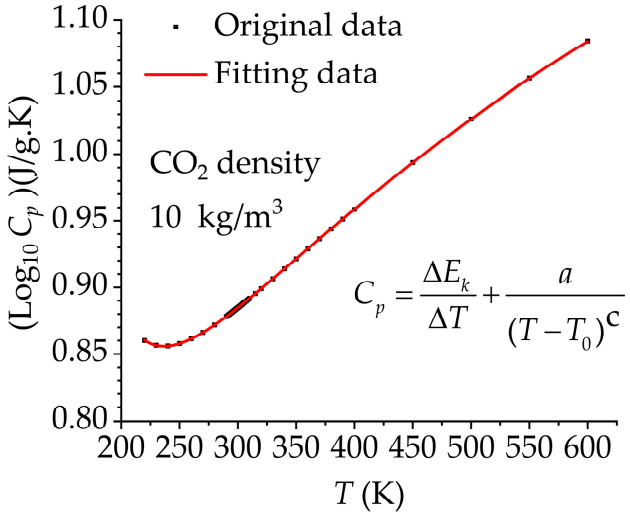

Figure 7. Original CO_2 heat capacity and fitting curve with the density of 10 kg/m^3 (with consideration of the molecular kinetic energy).

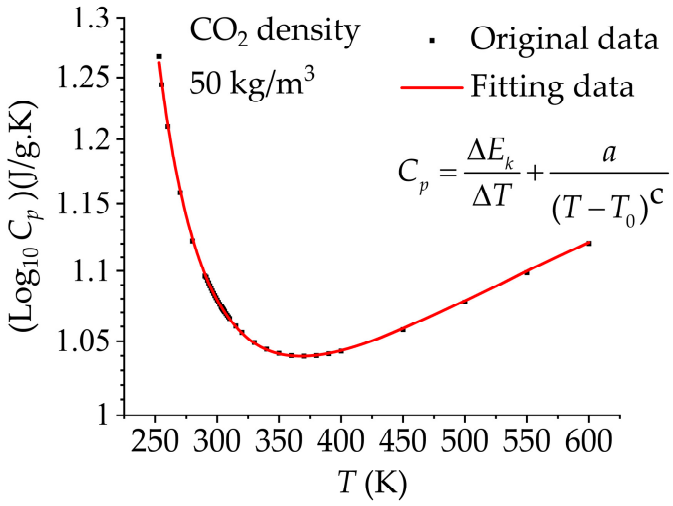

Figure 8. Original CO_2 heat capacity and fitting curve with the density of 50 kg/m^3 (with consideration of the molecular kinetic energy).

We used the software OriginPro to further verify the fitting precision of CO_2 heat capacity with densities of 1 kg/m^3, 467.6 kg/m^3 (critical density), and 1178 kg/m^3 (maximum density), as shown in Figures 9–11 and Table 3. We can see that the mean absolute relative

error (MARE) of the parameters in Equation (13) is less than 1/50 that of Equation (8) and that both the determination coefficients (*R-square*) and mean absolute relative error (*MARE*) reach excellent values. Equation (13) is demonstrated to well fit the variation in heat capacity with temperature. Therefore, we finally identify Equation (13) as the fitting Equation of CO_2 heat capacity as it fully considers the variation in molecular kinetic energy and potential energy. Figure 12 shows that the contribution ratio of the molecular kinetic energy to the total fitting CO_2 heat capacity (*Ratio*-C_p of E_k) increases with increases in temperature, and the maximum value reaches about 0.35, which proves the importance of considering the molecular kinetic energy.

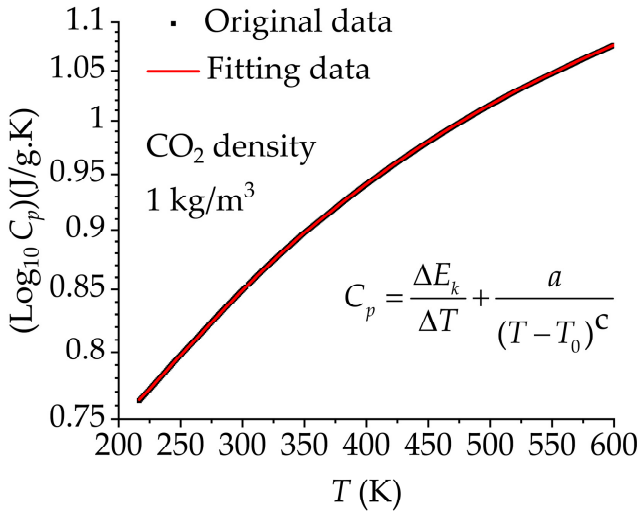

Figure 9. Original CO_2 heat capacity and fitting curve with the density of 1 kg/m^3 (with consideration of the molecular kinetic energy).

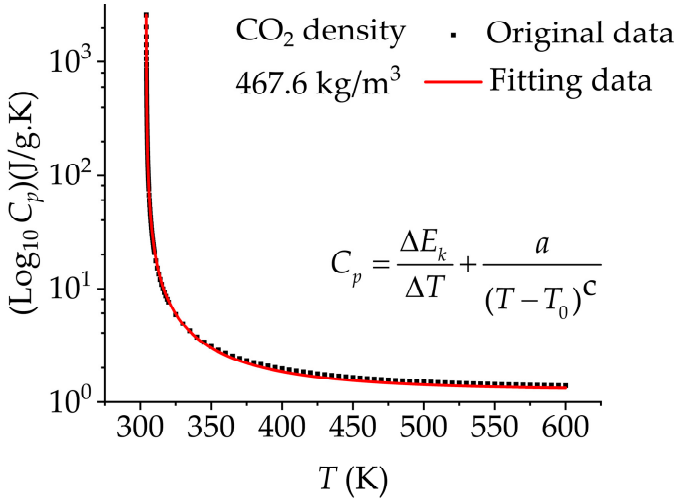

Figure 10. Original CO_2 heat capacity and fitting curve with the critical density of 467.6 kg/m^3 (with consideration of the molecular kinetic energy).

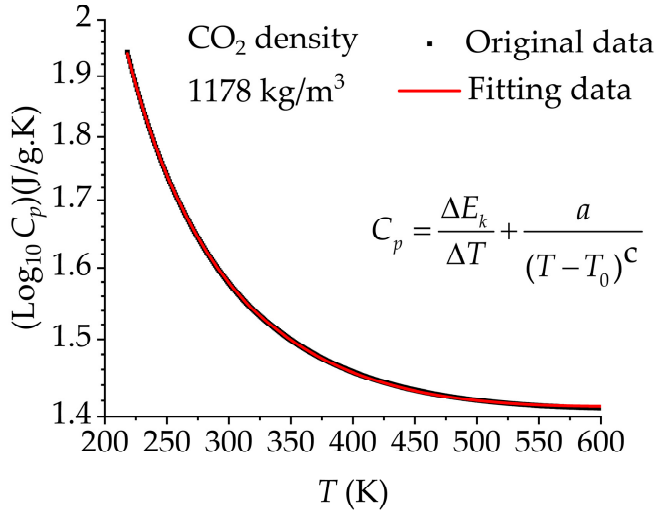

Figure 11. Original CO_2 heat capacity and fitting curve with the density of 1178 kg/m^3 (with consideration of the molecular kinetic energy).

Table 3. Fitting results for CO_2 heat capacity with different densities.

ρ kg/m^3	*a*	*c*	T_0	*R-Square*	*MARE* (%)
1	6.765	1.45845	128.1503	1	0.0001
10	71.9377	1.47141	134.17161	1	0.0004
50	76.80196	1.23533	190.82847	0.99947	0.0012
467.6	155.88611	1.12793	304.09746	0.99996	0.7123
1178	44.8895	0.79192	119.4896	0.99996	0.0002

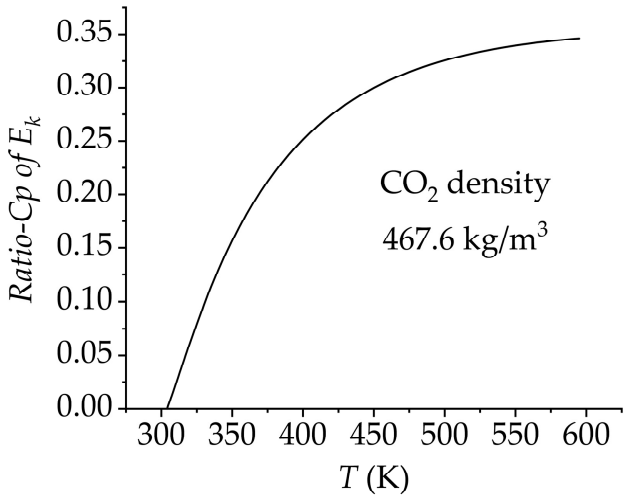

Figure 12. The contribution ratio of the molecular kinetic energy to total fitting CO_2 heat capacity with the critical density of 467.6 kg/m^3.

3. Fitting Equation Parameters Determination

During the first fitting, we find that the three parameters influence each other. Therefore, it is necessary to implement three rounds of fitting to identify *c*, T_0, and *a* in order. The first fitting determined the relationship between constant *c* and density; the second fitting determined the relationship between constant T_0 and density; the third fitting determined the relationship between constant *a* and density. The first and final fitting results of *a*, *c*, and T_0 are shown in Figures 13–15, which have an average determination coefficient of 0.99993, which indicates very high fitting precision.

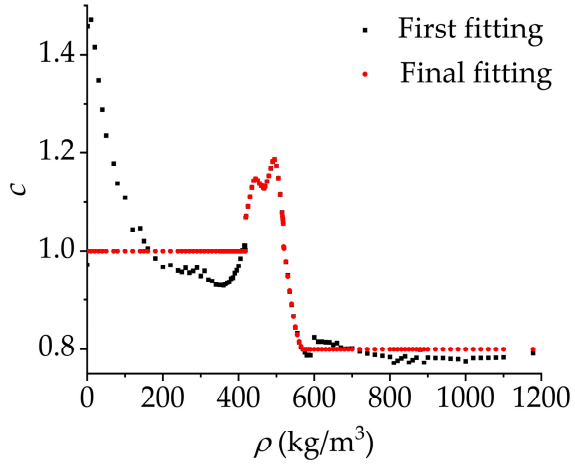

Figure 13. Variation of c with density during the first fitting.

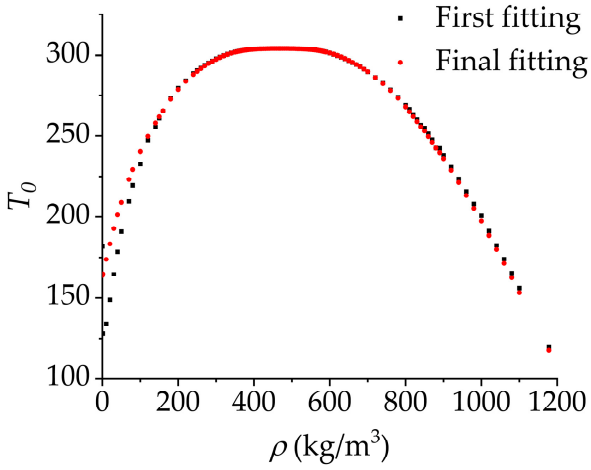

Figure 14. Variation of T_0 with density during the first fitting.

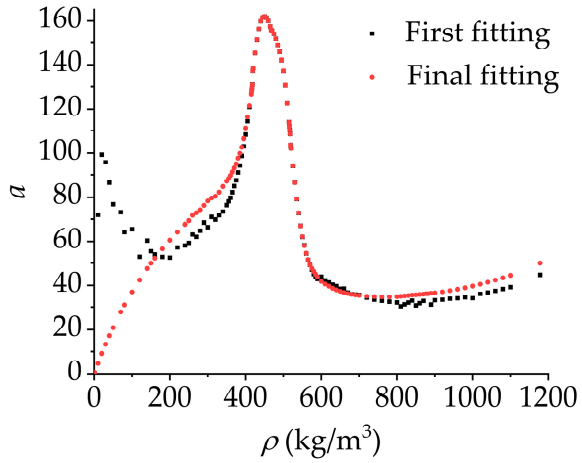

Figure 15. Variation of a with density during the first fitting.

It can be seen from the first fitting dot of Figure 14 that the variation of T_0 is more regular, which is totally different from that of a and c, especially when the density is low or high. The reason could be that more deviation from the critical density means a smaller change in molecular potential energy, which makes it difficult for the fitting parameters to reflect the influence of molecular potential energy on heat capacity. If we consider c as an impact factor for the influence of molecular potential energy on heat capacity, we

might obtain a larger c with larger molecular potential energy at the critical density point, whereas c tends to be a constant when the density is low or high. Therefore, we should simplify the fitting Equation of c. Existing multiple library functions in the OriginPro were compared and studied to finally identify the fitting Equation of c and the related parameters, as expressed as Equation (14) and shown in Table 4. The final fitting dot of Figure 13 shows the relationship between fitting c and density.

$$c = \begin{Bmatrix} 1 & (\rho \le 418) \\ A/\left[1+\sum_{i=1}^{5} A_i(|\rho - x_c|/500)^i\right] & (419 \le \rho \le 518) \\ A/\left[1+\sum_{i=1}^{5} A_i(|\rho - x_c|/500)^i\right] & (518 \le \rho \le 570) \\ 0.8 & (\rho \ge 570) \end{Bmatrix} \quad (14)$$

Table 4. Fitting parameters of c (*R-square* > 0.9999, *MARE* < 0.0001).

ρ kg/m^3	x_c	A	A_1	A_2	A_3	A_4	A_5
419–445	445	1.14733	−0.135	58.6	−560	−2143	45,108
445–467.6	467.6	1.12795	−0.12779	−22.8665	1322.2	−40188	430,658
467.6–495	467.6	1.12795	−0.62095	-19.3	840.2	−28050	318,116
495–518	495	1.18665	0.42544	74	−680	2790	0
518–570	570	0.8	−0.55794	−17.6784	−107.511	1356.378	0

When $\rho \le 418$ kg/m^3 or $\rho \ge 519$ kg/m^3, the maximum heat capacity can be calculated based on the NIST WebBook. However, in the transition zone where 418 kg/m^3 $\le \rho \le$ 519 kg/m^3, the maximum heat capacity cannot be calculated. Therefore, there should be a large mutation within or near the density range of 418–419 kg/m^3 and 518–519 kg/m^3. In this context, we adopt the linear interpolation method to calculate the heat capacity of the transition zone, expressed as Equation (15).

$$Cp = \begin{Bmatrix} Cp_{\rho=418} + (Cp_{\rho=419} - Cp_{\rho=418})(\rho - 418) & (418 \le \rho \le 419) \\ Cp_{\rho=518} + (Cp_{\rho=519} - Cp_{\rho=518})(\rho - 518) & (518 \le \rho \le 519) \end{Bmatrix} \quad (15)$$

In the fitting process, it is found that the heat capacity fitting precision is more sensitive to changes in T_0, whereas T_0 changes very regularly. Therefore, we then fit the T_0 through the piecewise Equation (16). Table 5 shows the fitting parameters. The final fitting dot of Figure 14 shows the relationship between fitting T_0 and density.

Table 5. Fitting parameters of T_0 (*R-square* > 0.9999, *MARE* < 0.0001).

ρ kg/m^3	x_c	A	A_1	A_2	A_3	A_4	A_5
0.01–250	250	290.17571	0.33243	0.2834	7.34123	−26.56616	40.9466
250–330	330	300.52514	0.11042	1.85179	−26.71893	209.13131	−543.8088
330–375	375	303.00611	0.06046	0.13587	6.2638	−67.77213	269.90062
375–418	418	303.94059	0.0181	0.28438	−5.80458	100.62786	−507.6728
419–445	445	304.09399	0.00631	0.10056	−0.81355	20.9428	−126.4
445–467.6	467.6	304.11792	−0.00025	−0.02075	0.64954	37.95686	−462
467.6–495	467.6	304.11792	−0.00019	−0.01384	−0.87259	70.33025	−644.07
495–518	495	304.08123	0.00786	0.09597	−0.2174	2.16398	0
519–570	519	303.92747	0.0188	0.01178	1.83036	−10.15248	47.55789
570–620	570	302.89499	0.0643	0.22867	1.40737	−1.70157	
620–700	620	299.90971	0.135	0.57585	−2.28116	18.71844	−46.52369
700–850	700	289.93954	0.25501	1.83235	−14.84521	67.05886	−97.84919
850–1178	850	253.00199	0.6462	0.74432	0.24847	1.81233	0

In the fitting process, it is found that the heat capacity fitting precision is more sensitive to changes in T_0, whereas T_0 changes very regularly. Therefore, we then fit the T_0 through the piecewise Equation (16). Table 5 shows the fitting parameters. The final fitting dot of Figure 14 shows the relationship between fitting T_0 and density.

$$T_0 = A / \left[1 + \sum_{i=1}^{5} A_i \left(|\rho - x_c| / 500 \right)^i \right] \quad (0.01 \le \rho \le 1178) \tag{16}$$

Based on the calculated c and T_0 by Equations (14) and (16), the equation is fitted for the third time, which brings in variations of a. This has a high determination coefficient of 0.99925, still indicating a very high fitting precision. Then a is fitted by the piecewise Equation (17). Table 6 shows the fitting parameters. The final fitting dot of Figure 14 shows the relationship between fitting a and density.

$$a = \left\{ \begin{array}{cc} (67.24968 + 167.4\rho)/(\rho + 354) & (0 \le \rho \le 250) \\ A / \left[1 + \sum\limits_{i=1}^{5} A_i \left(|\rho - \rho_0| / 500 \right)^i \right] & (250 \le \rho \le 1178) \end{array} \right\} \tag{17}$$

Table 6. Fitting parameters of a (*R-square* > 0.9999, *MARE* < 0.0001).

ρ kg/m^3	ρ_0	A	A_1	A_2	A_3	A_4	A_5
250–330	330	82.24941	2.17897	−77.69272	1477.057	−10,862.85	27,604.2
330–375	375	95.04348	1.86662	22.971	−945.3032	11,954.6	−49,742.9
375–418	375	95.04348	−3.58088	129.32	−4664.13	60,103.1	−264,235.5
419–445	445	161.57195	0.60004	38.45717	1152.5	−23,625.2	139,048
445–467.6	467.6	155.88555	−1.91731	−9.8931	2295	−52,762.5	423,919
467.6–495	467.6	155.88555	0.80828	−24.82	2681.87	−58,726.45	435,333
495–518	495	142.14881	2.91935	58.266	1210.6	−20,377.8	125,216.9
519–570	570	49.33043	−4.12187	−38.1146	306.7	−316.4	116.7
570–620	570	49.33043	4.29655	−91.66	2592.7	−31861	132,164
620–700	620	39.7411	1.49342	−10.76	92.021	−479.35	920.58
700–850	700	35.39488	0.40317	−4.7353	39.246	−165.635	238.462
850–1178	850	35.67187	−0.23465	0.04875	−2.13036	4.66409	−3.08148

4. Validation of Fitting Precision

Based on the fitting equations of a, c and T_0, we compile the C++ program to calculate the heat capacity and validate the results near the critical temperature point with temperatures of 304.1 K and 304.3 K. Figures 16 and 17 show the comparison result at the temperatures of 304.1 K and 304.3 K. Table 7 shows the points where the critical CO_2 heat capacities in the NIST WebBook and NIST REFPROP are predicted successfully using the fitting method. Through comparison with the NIST WebBook and NIST REFPROP data, the mean absolute relative errors (*MAREs*) were below 0.674% and 0.337%, respectively. The biggest *MARE* happens around the critical density, where the heat capacity and its change rate with density is high. There are various reasons for the *MARE*, and the main reason should be the measures taken for the fitting simplification, such as the assumption of the molecular kinetic energy density independence, the disregard of the influence of the intramolecular potential energy, and the mandatory assignment of c away from the critical density. Nevertheless, compared with the NIST REFPROP heat capacity, the fitting equation still has acceptably high accuracy. In addition, several traditionally unavailable heat capacities in the NIST WebBook and NIST REFPROP are well predicted, such as the point with a temperature of 304.1 K and densities of 435–445 kg/m^3 and 510–560 kg/m^3. The fitting result shows that the fitting method established in the article has better convergence in the heat capacity calculation. The detailed C++ program and fitting data is in the Supplementary Materials.

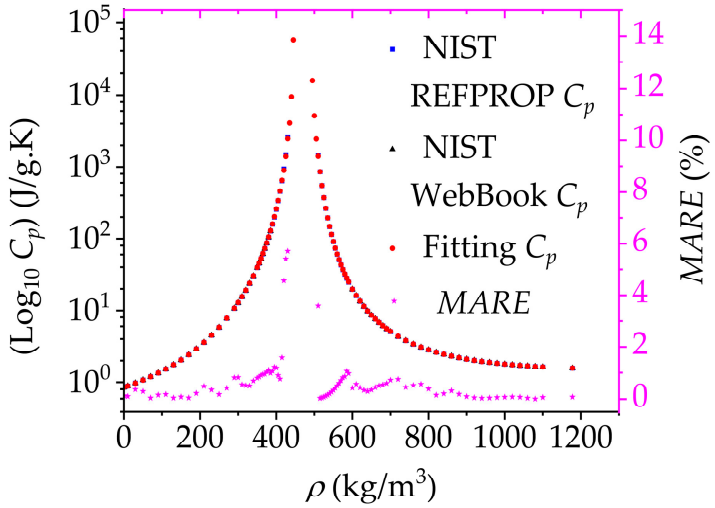

Figure 16. Variation in heat capacity with density at a temperature of 304.1 K.

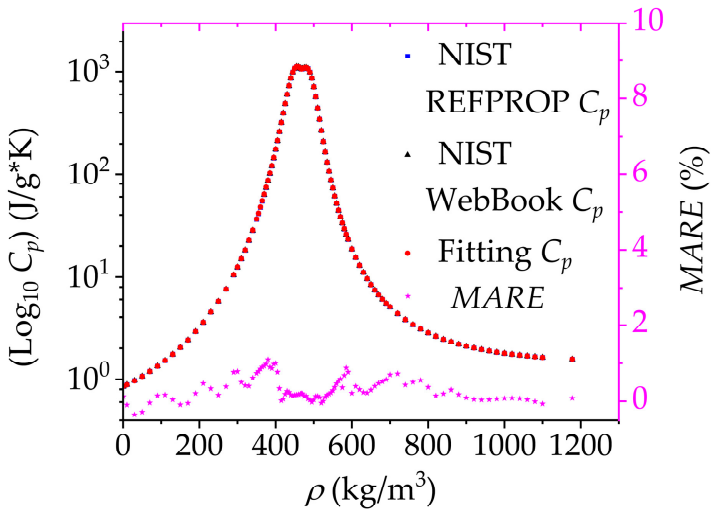

Figure 17. Variation in heat capacity with density at a temperature of 304.3 K.

Table 7. Points where critical CO_2 heat capacities are predicted successfully.

ρ (kg/m^3)	NIST WebBook C_p [44]	NIST REFPROP C_p	Fitting C_p	*MARE* (%)
385	128.03301	128.03301	129.29207	0.98339
390	Undefined	158.72872	160.41812	1.06433
430	Undefined	2614.91213	2465.61014	5.70964
435	Undefined	Undefined	4092.02132	Undefined
445	Undefined	Undefined	57112.40951	Undefined
450	Undefined	Undefined	Undefined	Undefined
490	Undefined	Undefined	Undefined	Undefined
495	Undefined	Undefined	15914.15082	Undefined
505	Undefined	Undefined	2453.76021	Undefined
510	Undefined	1457.67440	1405.32011	3.59163
560	Undefined	60.68897	60.98897	0.49432
565	50.74832	50.74832	51.04832	0.59115

5. Conclusions

Currently, existing accurate equations for the calculation of the heat capacities of carbon dioxide, nitrogen, methane, and water, are easy to diverge for heat capacity calculations near the critical temperature and pressure. To solve this problem, a fitting equation for heat

capacity with constant density was derived through analyses of the relationships among molecular potential energy, molecular kinetic energy, density, and temperature, which was further validated afterwards. The variations of the fitting parameters with density were fitted in order, which brings the carbon dioxide heat capacity variation with density and temperature. Based on this, a corresponding C++ program is compiled. Moreover, the relative error compared with the NIST WebBook data is identified to be within 1% with temperatures of 304.1 K and 304.3 K. In addition, for the areas where the NIST WebBook and NIST REFPROP data diverge easily, such as densities in the ranges 435–445 kg/m^3 and 510–560 kg/m^3 at 304.1 K, the fitting equation also made a good calculation. Moreover, due to the avoidance of complex intermediate calculation processes, the heat capacity calculation speed is greatly improved, which is more suitable for the calculation and simulation of large-scale engineering. Therefore, this fitting formula can be used as an effective supplement to the heat capacity calculation equation and as a prediction method for fluid heat capacity experimental data.

This paper has proved that the heat capacity variation near the critical point can be effectively fitted by the semi-empirical formula determined by molecular potential energy and kinetic energy. However, in order to reduce the complexity of the fitting formula and the difficulty of the fitting process, a simplified and relatively simple molecular potential energy equation was used that resulted in a decline in the fitting accuracy; this deficiency should be further studied in the future.

Supplementary Materials: The following supporting information can be downloaded at: https://www.mdpi.com/article/10.3390/pr11061605/s1, The C++ program for calculation of C_p and the detailed fitting data of in Figures 16 and 17.

Author Contributions: Conceptualization, M.L. and H.N.; methodology, M.L.; software, G.W.; validation, L.S. and X.C.; investigation, M.L.; resources, G.W.; data curation, L.S.; writing—original draft preparation, M.L.; writing—review and editing, M.L. and H.N.; visualization, X.C.; supervision, H.N.; project administration, G.W.; funding acquisition, M.L. All authors have read and agreed to the published version of the manuscript.

Funding: This research was funded by the Shandong Provincial Natural Science Foundation of China, grant number ZR2022ME077.

Institutional Review Board Statement: Not applicable.

Informed Consent Statement: Not applicable.

Data Availability Statement: The data presented in this study are available on request from the corresponding author.

Conflicts of Interest: The authors declare no conflict of interest.

References

1. Huang, M.; Kang, Y.; Wang, X.; Hu, Y.; Li, D.; Cai, C.; Liu, Y. Experimental investigation on the impingement characteristics of a self-excited oscillation pulsed supercritical carbon dioxide jet. *Exp. Therm. Fluid Sci.* **2018**, *94*, 304–315. [CrossRef]
2. Wang, R.; Ni, H.; Song, W.; Xiao, C. The development of fundamental research on supercritical carbon dioxide drilling. *Pet. Drill. Tech.* **2018**, *46*, 1–9.
3. Chen, H.; Hu, Y.; Kang, Y.; Wang, X.; Liu, F.; Liu, Y. Advantages of supercritical CO_2 compound fracturing in shale on fracture geometry, complexity and width. *J. Nat. Gas Sci. Eng.* **2021**, *93*, 104033. [CrossRef]
4. Kolle, J.J. Coiled-tubing drilling with supercritical carbon dioxide. In Proceedings of the SPE/CIM International Conference on Horizontal Well Technology, Calgary, AB, Canada, 6 November 2000.
5. Kolle, J.; Marvin, M. Jet-assisted coiled tubing drilling with supercritical carbon dioxide. In Proceedings of the ETCE/OMAE2000 Joint Energy Conference, New Orleans, LA, USA, 14–17 February 2000.
6. Zhang, X.; Lu, Y.; Tang, J.; Zhou, Z.; Liao, Y. Experimental study on fracture initiation and propagation in shale using supercritical carbon dioxide fracturing. *Fuel* **2017**, *190*, 370–378. [CrossRef]
7. Cai, C.; Kang, Y.; Wang, X.; Hu, Y.; Chen, H.; Yuan, X.; Cai, Y. Mechanism of supercritical carbon dioxide (SC-CO_2) hydro-jet fracturing. *J. CO_2 Util.* **2018**, *26*, 575–587. [CrossRef]
8. Li, X.; Feng, Z.; Han, G.; Elsworth, D.; Marone, C.; Saffer, D.; Cheon, D.-S. Breakdown pressure and fracture surface morphology of hydraulic fracturing in shale with H_2O, CO_2 and N_2. *Geomech. Geophys. Geo-Energy Geo-Resour.* **2016**, *2*, 63–76. [CrossRef]

9. Lyu, Q.; Tan, J.; Li, L.; Ju, Y.; Busch, A.; Wood, D.A.; Ranjith, P.G.; Middleton, R.; Shu, B.; Hu, C. The role of supercritical carbon dioxide for recovery of shale gas and sequestration in gas shale reservoirs. *Energy Environ. Sci.* **2021**, *14*, 4203–4227. [CrossRef]
10. Zhang, C.; Liu, S.; Ma, Z.; Ranjith, P. Combined micro-proppant and supercritical carbon dioxide (SC-CO_2) fracturing in shale gas reservoirs: A review. *Fuel* **2021**, *305*, 121431. [CrossRef]
11. Du, Y.; Wang, R.; Ni, H.; Huo, H.J.; Huang, Z.; Yue, W.M.; Zhao, H.; Zhao, B. Rock-breaking experiment with supercritical carbon dioxide jet. *J. China Univ. Pet.* **2012**, *36*, 93–96.
12. Du, Y.K.; Wang, R.H.; Ni, H.J.; Li, M.K.; Song, W.Q.; Song, H.F. Determination of rock-breaking performance of high-pressure supercritical carbon dioxide jet. *J. Hydrodyn. Ser. B* **2012**, *24*, 554–560. [CrossRef]
13. Tian, S.; He, Z.; Li, G.; Wang, H.; Shen, Z.; Liu, Q. Influences of ambient pressure and nozzle-to-target distance on SC-CO_2 jet impingement and perforation. *J. Nat. Gas Sci. Eng.* **2015**, *29*, 232–242. [CrossRef]
14. Wang, H.; Li, G.; Shen, Z.; Tian, S.; Sun, B.; He, Z.; Lu, P. Experiment on rock breaking with supercritical carbon dioxide jet. *J. Pet. Sci. Eng.* **2015**, *127*, 305–310. [CrossRef]
15. Huang, F.; Lu, Y.; Tang, J.; Ao, X.; Jia, Y. Research on erosion of shale impacted by supercritical carbon dioxide jet. *Chin. J. Rock Mech. Eng.* **2015**, *34*, 787–794.
16. Huang, F.; Hu, B. Macro/microbehavior of shale rock under the dynamic impingement of a high-pressure supercritical carbon dioxide jet. *RSC Adv.* **2018**, *8*, 38065–38074. [CrossRef]
17. Li, M.; Ni, H.; Xiao, C.; Wang, R. Influences of supercritical carbon dioxide jets on damage mechanisms of rock. *Arab. J. Sci. Eng.* **2018**, *43*, 2641–2658. [CrossRef]
18. Li, M.; Ni, H.; Wang, R.; Song, W. The effect of thermal stresses on the relation between rock failure and temperature and pressure of supercritical carbon dioxide jet. *Greenh. Gases-Sci. Technol.* **2018**, *8*, 218–237. [CrossRef]
19. Li, M.K.; Ni, H.J.; Wang, R.H.; Xiao, C.Y. Comparative simulation research on the stress characteristics of supercritical carbon dioxide jets, nitrogen jets and water jets. *Eng. Appl. Comput. Fluid Mech.* **2017**, *11*, 357–370. [CrossRef]
20. Li, M.; Wang, G.; Cheng, W.; Pu, S.; Ni, H.; Shi, X. Heat-fluid-solid coupling mechanism of supercritical carbon dioxide jet in rock-breaking. *Pet. Explor. Dev.* **2021**, *48*, 1450–1461. [CrossRef]
21. Li, M.; Ma, Y.; Guan, H.; Li, L. Development and experimental study of CO_2 expander in CO_2 supercritical refrigeration cycles. *Int. J. Green Energy* **2004**, *1*, 89–99. [CrossRef]
22. Zhang, X.; Wang, F.; Fan, X.; Duan, H.; Zhu, F. An investigation of heat pump system using CO_2/propane mixture as a working fluid. *Int. J. Green Energy* **2016**, *14*, 105–111. [CrossRef]
23. Li, M.; Ma, Y.; Gong, W.; Su, W. Analysis of CO_2 transcritical cycle heat pump dryers. *Dry. Technol.* **2009**, *27*, 548–554. [CrossRef]
24. Zhao, Z.; Che, D.; Wu, J.; Yao, S.; Zhang, K.; Lin, Y.; Ke, H. Numerical investigation on conjugate cooling heat transfer to supercritical CO_2 in vertical double-pipe heat exchangers. *Numer. Heat Transf. Part A Appl.* **2016**, *69*, 512–528. [CrossRef]
25. Maina, P.; Huan, Z. Effects of refrigerant charge in the output of a CO_2 heat pump. *Afr. J. Sci. Technol. Innov. Dev.* **2013**, *5*, 303–311. [CrossRef]
26. Lei, H. Performance comparison of H_2O and CO_2 as the working fluid in coupled wellbore/reservoir systems for geothermal heat extraction. *Front. Earth Sci.* **2022**, *10*, 819778. [CrossRef]
27. Plaksina, T.; White, C. Modeling coupled convection and carbon dioxide injection for improved heat harvesting in geopressured geothermal reservoirs. *Geotherm. Energy* **2016**, *4*, 2. [CrossRef]
28. Wu, Y.; Li, P. The potential of coupled carbon storage and geothermal extraction in a CO_2-enhanced geothermal system: A review. *Geotherm. Energy* **2020**, *8*, 19. [CrossRef]
29. Meshram, A.; Jaiswal, A.K.; Khivsara, S.D.; Ortega, J.D.; Ho, C.; Bapat, R.; Dutta, P. Modeling and analysis of a printed circuit heat exchanger for supercritical CO_2 power cycle applications. *Appl. Therm. Eng.* **2016**, *109*, 861–870. [CrossRef]
30. Sawalha, S.; Karampour, M.; Rogstam, J. Field measurements of supermarket refrigeration systems. Part I: Analysis of CO_2 trans-critical refrigeration systems. *Appl. Therm. Eng.* **2015**, *87*, 633–647. [CrossRef]
31. Ratnakar, R.; Dindoruk, B.; Livescu, S.; Gautam, S. A comparative study of the impact of the CO_2 properties on the thermal output of a geothermal well. In Proceedings of the SPE Improved Oil Recovery Conference, Virtual. 25–29 April 2022.
32. Cao, Y.; Li, P.; Qiao, Z.; Ren, S.; Si, F. A concept of a supercritical CO_2 Brayton and organic Rankine combined cycle for solar energy utilization with typical geothermal as auxiliary heat source: Thermodynamic analysis and optimization. *Energy Rep.* **2022**, *8*, 322–333. [CrossRef]
33. Ezekiel, J.; Adams, B.M.; Saar, M.O.; Ebigbo, A. Numerical analysis and optimization of the performance of CO_2-Plume Geothermal (CPG) production wells and implications for electric power generation. *Geothermics* **2022**, *98*, 102270. [CrossRef]
34. Liao, S.; Zhao, T. Measurements of heat transfer coefficients from supercritical carbon dioxide flowing in horizontal mini/micro channels. *Trans. -Am. Soc. Mech. Eng. J. Heat Transf.* **2002**, *124*, 413–420. [CrossRef]
35. Yoon, S.H.; Kim, J.H.; Hwang, Y.W.; Kim, M.S.; Min, K.; Kim, Y. Heat transfer and pressure drop characteristics during the in-tube cooling process of carbon dioxide in the supercritical region. *Int. J. Refrig.* **2003**, *26*, 857–864. [CrossRef]
36. Chen, L.; Deng, B.-L.; Zhang, X.-R. Experimental study of trans-critical and supercritical CO_2 natural circulation flow in a closed loop. *Appl. Therm. Eng.* **2013**, *59*, 1–13. [CrossRef]
37. Ni, H.; Li, M.; Wang, R.; Wang, P. Apparatus and method of generating electricity using carbon dioxide. ZL 201510191021.0,tex-twidth 2 March 2016.

38. Ni, H.; Li, M.; Wang, R.; Wang, P. Apparatus and method for geothermal exploitation using supercritical carbon dioxide. ZL 201510188899.9, 24 September 2016.
39. Bagheri, H.; Hashemipour, H.; Rahimpour, E.; Rahimpour, M.R. Particle size design of acetaminophen using supercritical carbon dioxide to improve drug delivery: Experimental and modeling. *J. Environ. Chem. Eng.* **2021**, *9*, 106384. [CrossRef]
40. Notej, B.; Bagheri, H.; Alsaikhan, F.; Hashemipour, H. Increasing solubility of phenytoin and raloxifene drugs: Application of supercritical CO_2 technology. *J. Mol. Liq.* **2023**, *373*, 121246. [CrossRef]
41. Bagher, H.; Notej, B.; Shahsavari, S.; Hashemipour, H. Supercritical carbon dioxide utilization in drug delivery: Experimental study and modeling of paracetamol solubility. *Eur. J. Pharm. Sci.* **2022**, *177*, 106273. [CrossRef]
42. Span, R.; Wagner, W. A new equation of state for carbon dioxide covering the fluid region from the triple-point temperature to 1100 K at pressures up to 800 MPa. *J. Phys. Chem. Ref. Data* **1996**, *25*, 1509–1596. [CrossRef]
43. Kunz, O.; Wagner, W. The GERG-2008 wide-range equation of state for natural gases and other mixtures: An expansion of GERG-2004. *J. Chem. Eng. Data* **2012**, *57*, 3032–3091. [CrossRef]
44. NIST Chemistry WebBook. Available online: https://webbook.nist.gov/chemistry (accessed on 10 February 2023).
45. Yang, C.; Yang, C. Critical point in liquid-gas transitions. *Phys. Rev. Lett.* **1964**, *13*, 303. [CrossRef]
46. Botch, W.; Fixman, M. Sound absorption in gases in the critical region. *J. Chem. Phys.* **1965**, *42*, 199–204. [CrossRef]
47. Orkoulas, G.; Fisher, M.E.; Üstün, C. The Yang–Yang relation and the specific heats of propane and carbon dioxide. *J. Chem. Phys.* **2000**, *113*, 7530–7545. [CrossRef]
48. Zhang, Y.; Yang, J.; Yu, Y.-X. Dielectric constant and density dependence of the structure of supercritical carbon dioxide using a new modified empirical potential model: A Monte Carlo simulation study. *J. Phys. Chem. B* **2005**, *109*, 13375–13382. [CrossRef]
49. Möller, D.; Fischer, J. Determination of an effective intermolecular potential for carbon dioxide using vapour-liquid phase equilibria from NpT+ test particle simulations. *Fluid Phase Equilibria* **1994**, *100*, 35–61. [CrossRef]
50. Stubbs, J.M.; Siepmann, J.I. Binary phase behavior and aggregation of dilute methanol in supercritical carbon dioxide: A Monte Carlo simulation study. *J. Chem. Phys.* **2004**, *121*, 1525–1534. [CrossRef]
51. Yigzawe, T.M.; Sadus, R.J. Intermolecular interactions and the thermodynamic properties of supercritical fluids. *J. Chem. Phys.* **2013**, *138*, 194502. [CrossRef]
52. Mairhofer, J.; Sadus, R.J. Thermodynamic properties of supercritical nm Lennard-Jones fluids and isochoric and isobaric heat capacity maxima and minima. *J. Chem. Phys.* **2013**, *139*, 154503. [CrossRef]
53. Harris, J.G.; Yung, K.H. Carbon dioxide's liquid-vapor coexistence curve and critical properties as predicted by a simple molecular model. *J. Phys. Chem.* **1995**, *99*, 12021–12024. [CrossRef]
54. Colina, C.; Olivera-Fuentes, C.; Siperstein, F.; Lisal, M.; Gubbins, K. Thermal properties of supercritical carbon dioxide by Monte Carlo simulations. *Mol. Simul.* **2003**, *29*, 405–412. [CrossRef]
55. Meng, L.; Duan, Y.-Y. Determination of energy parameters using the extended 2CLJ model. *J. Eng. Thermophys.* **2007**, *28*, 13–16.
56. Wang, S.; Zhang, Y.; He, M.-G. Potential energy function and the secondvirial coefficients of the linera molecules. *J. Eng. Thermophys.* **2012**, *33*, 199–202.
57. Ishii, R.; Okazaki, S.; Okada, I.; Furusaka, M.; Watanabe, N.; Misawa, M.; Fukunaga, T. Density dependence of structure of supercritical carbon dioxide along an isotherm. *J. Chem. Phys.* **1996**, *105*, 7011–7021. [CrossRef]
58. Zarkova, L.; Hohma, U.; Damyanova, M. Potential of binary interactions and thermophysical properties of chlorine in a gas phase. *J. Optoelectron. Adv. Mater.* **2005**, *7*, 2385–2389.
59. Zarkova, L. An isotropic intermolecular potential with temperature dependent effective parameters for heavy globular gases. *Mol. Phys.* **1996**, *88*, 489–495. [CrossRef]
60. Potoff, J.J.; Panagiotopoulos, A.Z. Critical point and phase behavior of the pure fluid and a Lennard-Jones mixture. *J. Chem. Phys.* **1998**, *109*, 10914–10920. [CrossRef]
61. Song, X.-S.; Linghu, R.-F.; Li, D.-H.; Yan, A.-Y. Total internal partition sums for the carbon dioxide in the temperature range 20~6000K. *J. At. Mol. Phys.* **2007**, *24*, 647–652.
62. McDowell, R.S. Rotational partition functions for linear molecules. *J. Chem. Phys.* **1988**, *88*, 356–361. [CrossRef]
63. Chedin, A. The carbon dioxide molecule: Potential, spectroscopic, and molecular constants from its infrared spectrum. *J. Mol. Spectrosc.* **1979**, *76*, 430–491. [CrossRef]